



Optimal control of a road racing motorcycle on a three-dimensional closed track

L. Leonelli & D. J. N. Limebeer

To cite this article: L. Leonelli & D. J. N. Limebeer (2019): Optimal control of a road racing motorcycle on a three-dimensional closed track, *Vehicle System Dynamics*, DOI: [10.1080/00423114.2019.1617886](https://doi.org/10.1080/00423114.2019.1617886)

To link to this article: <https://doi.org/10.1080/00423114.2019.1617886>



Published online: 30 May 2019.



Submit your article to this journal



Article views: 16



View Crossmark data



Optimal control of a road racing motorcycle on a three-dimensional closed track

L. Leonelli^a and D. J. N. Limebeer^{b,c,d}

^aDepartment of Engineering Enzo Ferrari, University of Modena and Reggio Emilia, Modena, Italy;

^bDepartment of Electrical & Electronic Engineering Science, University of Johannesburg, Johannesburg, South Africa;

^cDepartment of Electrical, Electronic and Computer Engineering, University of Pretoria, Pretoria, South Africa;

^dDepartment of Engineering Science, University of Oxford, Oxford, UK

ABSTRACT

The primary aim of this work is to validate dynamic minimum-lap-time optimal control simulations for a sports motorcycle on a 3D track. The racing line and rider inputs are optimised, while recognising the geometric features of a three-dimensional (3D) closed-circuit track, which is described in terms of curvilinear coordinates. A simple vehicle model is developed, which includes longitudinal weight transfer effects and a Magic Formula (MF) tyre description. The minimum-lap-time optimal control problem (OCP) is solved using a direct transcription technique that is based on orthogonal collocation. Detailed comparisons are made between experimental data and optimal theoretical predictions. The influences of the 3D features of the track are highlighted and discussed. The minimum-lap-time handling properties of the vehicle are also analysed.

ARTICLE HISTORY

Received 3 February 2019

Revised 22 April 2019

Accepted 4 May 2019

KEYWORDS

Motorcycle dynamics;
optimal control;
minimum-lap-time
simulation; trajectory
optimisation

1. Introduction

The importance of lap-time minimisation in motor sport is self-evident. As a consequence, a great deal of research has been dedicated to this topic. These investigations began with cars [1,2], where quasi-static arguments are used to generate velocity profiles over a given two-dimensional race track [3]. In these studies, a pre-imposed racing line is divided into a number of sections, and the associated vehicle trajectory is decomposed into a sequence of quasi-static equilibria. The tyre lateral forces are obtained from the imposed race line curvature, as a function of the vehicle speed, with the maximum longitudinal acceleration deduced from the available tyre forces. This approach can provide feasible results, while also being capable of accommodating a complex vehicle model. However, it provides no information about the transient behaviour of the vehicle or the optimal racing line.

To address these shortcomings, optimal control techniques can be employed that minimise the time required to complete a lap. By describing the lap in terms of the distance travelled along the track centre line, the OCP becomes a fixed horizon problem. Direct solution methods have been widely employed, because they do not require co-state equations, and they are able to deal with complex constraint sets. An early example is [4], where

a gradient descent method is used to solve a minimum-time problem for a point-mass car model with MF tyres. Minimum-lap-time trajectories have been computed for a 7-degrees-of-freedom (DOF) Formula One car model using a parallel shooting method [5]. In [6] a solution strategy is proposed that uses barrier functions to impose path constraints. Lane change and U-turn manoeuvres, as well as complete laps, are analysed in [7] using a 3-DOF car model with linear friction ellipse limited tyres. The states and controls are evaluated on a fixed centre line mesh, with intermediate values obtained by interpolation as required. The resulting nonlinear programme (NLP) is solved using a sequential quadratic programming algorithm. A direct collocation scheme and an NLP algorithm are used in [8] to optimise vehicle setup parameters for a 3-DOF model of a F1 car with MF tyres. In a development of this work, the flat-track assumption used in [8,9], is replaced with a three-curvature-variable description of the track [10]. The associated minimum-time OCP is solved with a pseudospectral method based on Legendre–Gauss–Radau (LGR) collocation and Radau’s integration formula [11].

Modelling complexities, as well as a comparatively lower demand, have meant that minimum-lap-time manoeuvring for motorcycles has received somewhat less attention. Nevertheless, both transient and quasi-static analysis methods for two-wheeled vehicles have been reported in the literature. The approach first presented in [12] uses a mixed symbolic-numerical indirect optimisation method. Starting from a track centre line description, a symbolic multibody motorcycle model is developed using the MapleTM library [13]. Penalty functions are used to impose inequality constraints. The optimal solution is found by solving a two-point boundary value problem (BVP) derived from the first-order optimality conditions, which are discretised by finite differences, and then solved using the numerical scheme described in [14]. Symbolic calculations are used to evaluate the required derivatives for the BVP, as well as the associated adjoint equations. The complexity of typical motorcycle model equations of motion (EoM) prevents the resulting mass matrix from being inverted symbolically. As a consequence, the solver deals with the dynamics in implicit form, as opposed to most direct method solvers, such as [15,16]. Applications of this method include the performance optimisation of racing motorcycles [17], as well as comparative study with experimental data [18]. In order to make motorcycle optimal control problems more manageable, it has been proposed that a pre-assigned racing line is used [19]. In this case, the problem becomes one of finding the minimum-time trajectory for a point-mass vehicle constrained to follow a prescribed path subjected to acceleration limits. All the aforementioned literature make use of a flat-track assumption, in combination with friction ellipse limited tyres. The effect of road banking on motorcycle stability during cornering has been studied in [20] by means of frozen time eigenvalues analysis, but no information on the related minimum time manoeuvring is provided. The work presented here will focus on minimum-lap-time optimal control, using direct transcription and a simplified motorcycle model with MF tyres. The track model used is three-dimensional.

Section 2 provides an overview of the geometric description of the 3D track chosen in this case study. Section 3 describes the vehicle model, highlighting the features that make it suitable for optimal control. In Section 4 the definition and solution of the OCP are discussed, with a focus on the specific issues presented by the motorcycle problem. Finally, in Section 5, the minimum-lap-time trajectories computed on the 3D track are validated against experimental data and then compared with those obtained with a flat-track

assumption. Some remarks on tyre grip usage for minimum-lap-time manoeuvring are also given. Conclusions are provided in Section 6.

2. Track model

A road model is required in vehicular optimal control problems so that road-related path constraints can be incorporated in the OCP. Track-related path constraints are enforced by ensuring that the vehicle remains in contact with the road, with its tyre ground contact points within the track boundaries. The basic idea is to describe the 3D track surface as a ‘ribbon’, which is a differential geometric object describable by means of three-curvature variables. The track modelling procedure adopted here follows the curvilinear coordinate description presented in [10,21], where a detailed account can be found.

We will represent the track centre line \mathcal{C} as the three-dimensional arc of a curve in space. The road is described by a *ribbon*, which can be created by augmenting the track centre line with notions of ‘width’ and ‘camber’. A parametric representation of the ribbon is

$$\nabla = \{\mathbf{r}(s, n) = \mathbf{x}(s) + \mathbf{n}(s)n \in \mathbb{R}^3 : s \in [s_0, s_f], n \in [n_l(s), n_r(s)]\}, \quad (1)$$

in which $\mathbf{x}(s)$ is the ribbon’s *spine curve* (i.e. the track centre line), s is the arc length, and n is the lateral offset from the spine curve in the ribbon plane. The origin of the moving trihedron travels along $\mathbf{x}(s)$. The left- and right-hand road boundaries are described by n_l and n_r respectively. Lateral displacements of the vehicle on the ribbon surface are measured by n in the direction of the unit vector $\mathbf{n}(s)$ normal to the direction of travel. The width of the ribbon (track) at each s is given by $|n_r - n_l|(s)$.

The orientation of the moving triad can be described with three rotations – the related angles are the Euler angles Ψ , Θ , and Φ in the $z-y-x$ (yaw, pitch, and roll) convention, and is given by $R_R = R_z(\Psi)R_y(\Theta)R_x(\Phi)$ [21].

The angular rate vector $\boldsymbol{\Omega}^\nabla$ is a vector in \mathbb{R}^3 , which has a skew-symmetric matrix representation $S(\boldsymbol{\Omega}^\nabla)$ that can be expressed in the ribbon trihedron as

$$\boldsymbol{\Omega}^\nabla = \begin{bmatrix} \Omega_x \\ \Omega_y \\ \Omega_z \end{bmatrix}, \quad S(\boldsymbol{\Omega}^\nabla) = \begin{bmatrix} 0 & -\Omega_z & \Omega_y \\ \Omega_z & 0 & -\Omega_x \\ -\Omega_y & \Omega_x & 0 \end{bmatrix}, \quad (2)$$

where Ω_x , Ω_y , and Ω_z are known as the *relative torsion*, the *normal curvature*, and the *geodesic curvature*, respectively.

Once the generalised curvature vector $\boldsymbol{\Omega}^\nabla$ and the widths n_r, n_l are given as a function of the curvilinear abscissa s , the ribbon can be computed by integration, given the initial conditions $\mathbf{x}(s_0)$ and $R_R(s_0)$ [21].

2.1. Autodromo del mugello

As a consequence of the ribbon assumption, all track model transverse cross sections are straight lines. Therefore, a track model can be derived using boundary information only. A description of the track boundaries can be assembled from satellite imagery and GPS data. Several online databases are available, which provide the required latitude–longitude–elevation information. The latitude–longitude–elevation data can then be

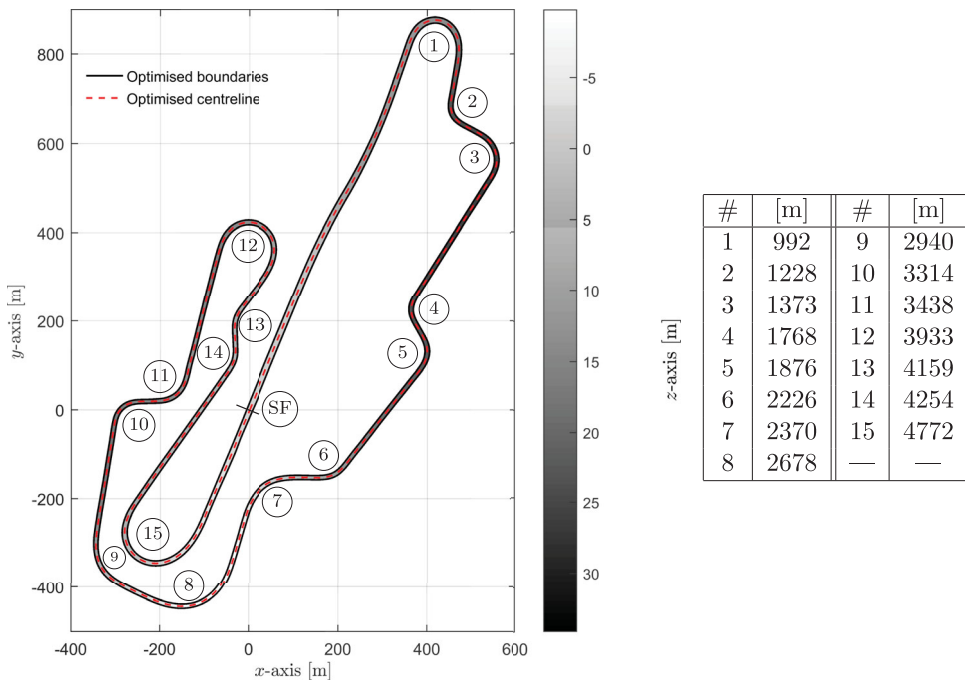


Figure 1. Plan view of the Mugello Circuit. The table gives the distances to each corner from the start–finish line. The track length is approximately 5245 m.

converted into Cartesian coordinates with the Mercator projection [22]. In order to negate the effect of data measurement noise, and to enforce cyclic constraints on the computed Euler angles, a filtering procedure based on an auxiliary OCP has been employed [21]. The Euler angle second derivatives, and the track half-width derivatives were chosen as the control variables in this auxiliary OCP. The objective function to be minimised is defined as the (weighted) least-squares distance between the computed ribbon and one obtained by means of finite differentiation. The weighting parameters are chosen in order to find a compromise between modelling accuracy and smoothness in the track curvatures. Cyclic track closure constraints are set as boundary conditions for the auxiliary OCP.

A model of the Autodromo del Mugello in Florence, Italy, is presented in Figure 1. The centre line and boundaries are obtained from the OCP calculation described above. The reference system has its origin at the centre line of the start–finish (S–F) line, the x -axis is parallel to the equator, while the z -axis points downwards. The track is traversed in a clockwise direction and contains three U-turns (corners 1, 12, 15), a double right-hand bend (corners 8 and 9), and five chicanes (corners 2–3, 4–5, 6–7, 10–11, and 13–14). The main straight is 1112 m long, the average track width is 11 m, and the lap distance along the spine is 5243 m.

The track curvatures and the Euler angles are shown in Figure 2. The effect of the optimal filtering procedure is clearly visible: the black solid curves are smoothed and cyclic, while the dashed curves were obtained by finite differentiation. It can be seen that for corners (1, 8–9, 12, 15) the camber angle Φ has the same sign as the geodetic curvature Ω_z ,

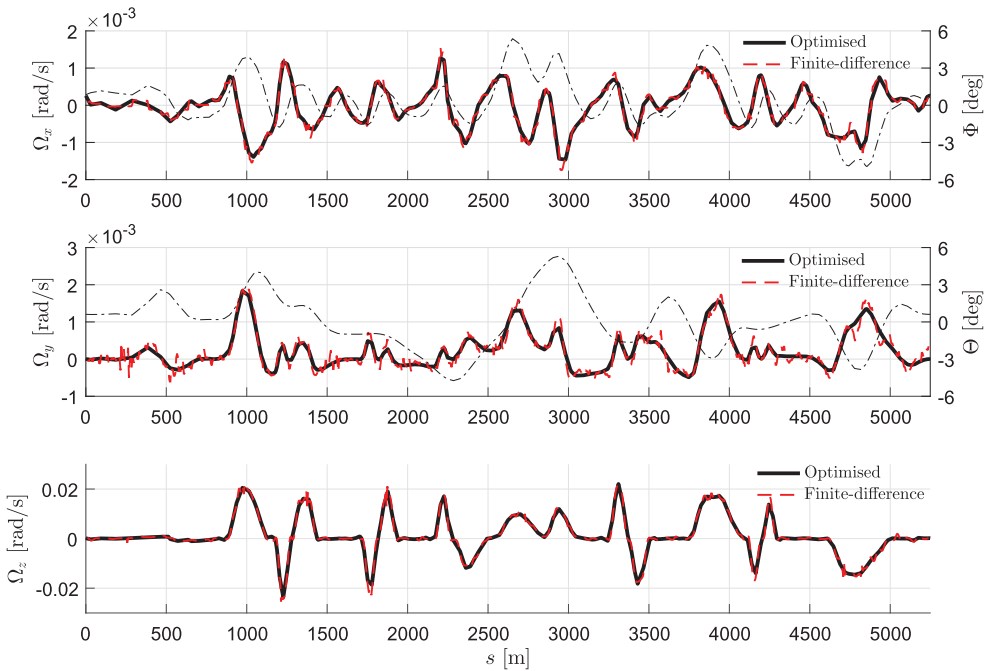


Figure 2. Curvatures and Euler angles for the Mugello Circuit. The track camber angle is Φ and is shown as a dot-dash curve in the top figure; the track gradient is Θ (positive uphill) and is shown as a dot-dash plot in the central figure.

this means that the road surface is positively cambered towards the centre of the corners. The chicanes have small camber angles.

The lowest point on the circuit (10.5 m below S-F line) is located just before corner 8 and is followed by an uphill stretch through corners 8 and 9. The main straight and corner 1 are uphill too. Track elevation is then lost on the decent through chicanes 2–3, 4–5, 6–7, and down to turn 8. The track has a crest close to the end of the main straight as can be seen in the Ω_y plot at approximately 500 m after the S-F line.

3. Vehicle model

The motorcycle model proposed here is based on the well known Whipple bicycle [21,23–25]. While several modifications have been introduced in order to make it more representative of a racing motorcycle, the essential features of the model remain unchanged. As shown in Figure 3, the model comprises four bodies: the main frame (including engine, rider and swingarm), the rear wheel, the front wheel and the steering assembly. A suspension is not included, as the associated closed-loop kinematics would make the EoM too difficult to solve for optimal control purposes. When the vehicle model is combined with the road model, it will be assumed that both wheel ground contact points are on the same track tangent plane, which is not necessarily horizontal. The motorcycle geometry is described by means of three fundamental parameters l_r , l_f , l_s : the orthogonal distance between the rear wheel hub and the steering axis; the steering offset; and the fork length respectively (see also Section 7.7 in [21]). The longitudinal and vertical distances

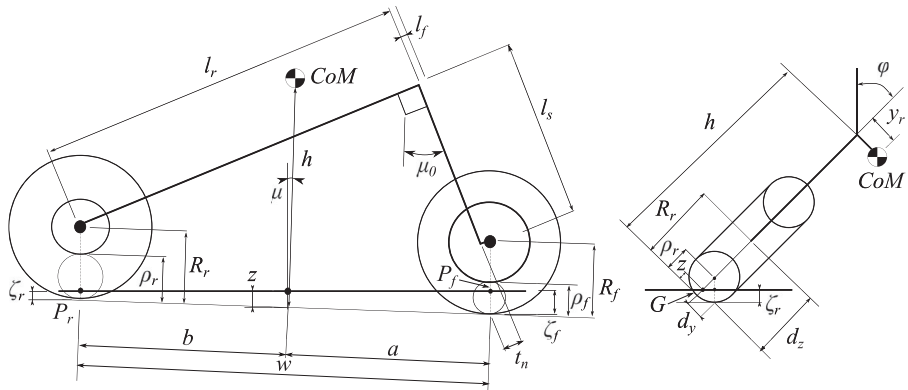


Figure 3. The motorcycle model in a generic configuration.

between the rear wheel ground contact point and the vehicle's centre of mass (CoM) are b and h respectively. Quantities such as the wheelbase w , the (static) caster angle μ_0 , and the normal trail t_n are easily derived.

The motorcycle's configuration is described in terms of three independent variables: the roll angle φ , the pitch angle μ , and the steer angle δ (around the steering axis). See Figure 3.

The orientation of the front assembly with respect to the vehicle mid-plane derives from a roll–pitch–steer series of rotations given by $R_x(\varphi)R_y(\mu + \mu_0)R_z(\delta)$. By equating this expression to the yaw–roll–pitch angles for the front wheel $R_z(\delta_f)R_x(\varphi_f)R_y(\mu_f)$, the front wheel angles are found to be

$$\begin{aligned}\delta_f &= \arctan\left(\frac{\sin \delta \cos (\mu + \mu_0)}{\cos \varphi \cos \delta - \sin \varphi \sin (\mu + \mu_0) \sin \delta}\right), \\ \varphi_f &= \arcsin(\sin \varphi \cos \delta + \cos \varphi \sin \delta \sin (\mu + \mu_0)), \\ \mu_f &= \arctan\left(\frac{\sin (\mu + \mu_0) \cos \delta - \sin \varphi \sin \delta}{\cos \varphi \cos (\mu + \mu_0)}\right).\end{aligned}\quad (3)$$

The caster angle (in absolute coordinates) is obtained by adding the nominal caster angle μ_0 to the pitch rotation angle of the whole vehicle with respect to the road μ . The bicycle's yaw angle and absolute location are cyclic coordinates. However, since no ground contact constraint has as yet been introduced, the vertical positioning of the bike body with respect to the road plane must also be described. The intersection point of the CoM projection along the motorcycle mid-plane and the road plane is denoted G . The vertical distance in the motorcycle mid-plane between G and the CoM projection in static trim is the variable z . The height of the CoM above the road plane is given by $h_G(t) = h \cos(\mu(t)) - z(t)$. Since h_G and the pitch angle μ of the motorcycle with respect to the road plane are time dependent variables, tyre deformations can be evaluated as functions of time. The contact point kinematics used here assume toroidal tyres, whose un-deformed contact point coordinates (in the unspun, road parallel, wheel hub reference frame) are described by

$$\begin{aligned}d_y &= \rho_r \sin(\varphi), \\ d_z &= R_r - \rho_r(1 - \cos(\varphi)).\end{aligned}\quad (4)$$

The same expression holds for the front wheel, but with parameters ρ_f , R_f and φ_f . The wheel ground contact points $P_{f,r}$ are calculated by considering the intersection between the road plane and the (un-deformed) toroidal tyre profiles. The vertical tyre deformations $\zeta_{f,r}$ are evaluated along a line perpendicular to the road plane, and passing through the wheel hubs:

$$\begin{aligned}\zeta_f &= \rho_f + ((b - w)s_\mu - c_\mu R_f + z)c_\varphi + (s_{\mu_0}R_f\delta - t_n\delta - y_r)s_\varphi + (R_f - \rho_f)c_{\varphi_f}, \\ \zeta_r &= \rho_r - s_\varphi y_r + ((R_r - h)(1 - c_\mu) + bs_\mu - \rho_r + z)c_\varphi.\end{aligned}\quad (5)$$

To accommodate the effect of the rider leaning away from the vehicle's central plane during cornering, an additional lateral displacement y_r , between the CoM and the motorcycle mid-plane, is included as a given function of the vehicle roll angle φ . See Appendix. The steering motion on a road racing motorcycles is usually 'small' ($|\delta| < 10^\circ$). As a consequence, from a dynamics standpoint, one can assume that the motorcycle can be treated as a single rigid body. This assumption leads to a significant reduction in the complexity of the resulting EoM. Also, the inertia matrix for a rigid body in body-fixed coordinates is constant and easily invertible.

3.1. Vehicle tracking

Using the ideas introduced in Section 2, any point lying on the ribbon surface can be located in terms of the distance travelled along the spine $s(t)$, and a lateral displacement $n(t)$ from it. To solve optimal control problems, we need to track the vehicle's CoM position on the track. We will do this by tracking the road-plane projection G of the CoM along the vehicle's plane of symmetry. The longitudinal u_G , lateral v_G , and vertical w_G velocities of G in the spine reference frame can be calculated using [21]

$$\begin{bmatrix} u_G \\ v_G \\ w_G \end{bmatrix} = \dot{s} \begin{bmatrix} v \\ \tau \\ \kappa \end{bmatrix} \times \begin{bmatrix} 0 \\ n \\ 0 \end{bmatrix} + R_R^T \begin{bmatrix} \dot{s} \\ \dot{n} \\ 0 \end{bmatrix} = \begin{bmatrix} \dot{s}(1 - n\kappa) \\ \dot{n} \\ n\dot{s}\tau \end{bmatrix}, \quad (6)$$

The vehicle's heading angle can be described in terms of the angle between the spine tangent vector t , and the intersection angle between vehicle's plane of symmetry and the road plane. The vehicle heading angle $\xi(t)$ is thus a rotation around a z -axis normal to the road surface, as depicted in Figure 4. The vehicle roll angle $\varphi(t)$ is defined as a rotation around a yawed x -axis (in the road surface), with the pitch rotation μ applied last. Therefore, the (absolute) orientation of the vehicle body-fixed reference frame (subscript B), is given by the product of road plane orientation matrix R_R with the yaw-roll-pitch series of rotations $R_B = R_R R_z(\xi) R_x(\varphi) R_y(\mu)$. In other words, the vehicle is described as a rigid body that has 6-DOF, three translations s, n, z and three rotations ξ, φ, μ with respect to the race track centre line.

The vehicle's angular velocities $\omega = [\omega_x, \omega_y, \omega_z]^T$, in the body-fixed reference frame, are the components of the skew-symmetric matrix $R_B^T \dot{R}_B$, recalling the relationship between road-plane angular velocities given in (2). These are then combined with the curvatures

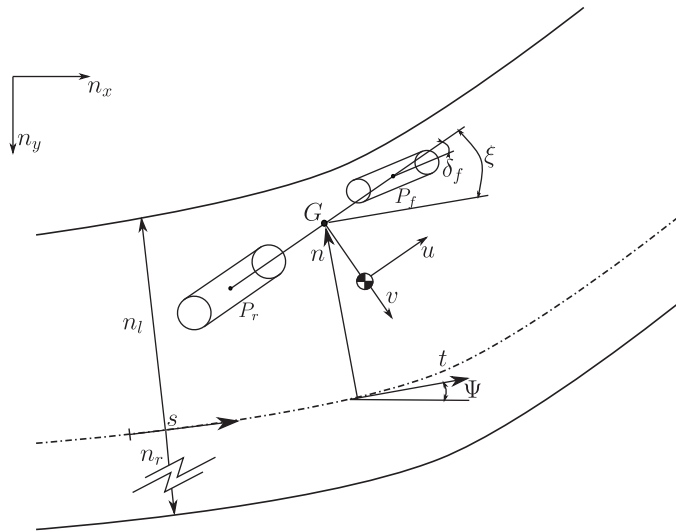


Figure 4. Motorcycle model positioning on the track.

$[\Omega_x, \Omega_y, \Omega_z]^T = \dot{s}[\nu, \tau, \kappa]^T$ to give

$$\begin{bmatrix} \omega_x \\ \omega_y \\ \omega_z \end{bmatrix} = \begin{bmatrix} ((-\kappa c_\varphi - s_\varphi(\nu s_\xi - \tau c_\xi))s_\mu + c_\mu(\tau s_\xi + \nu c_\xi))\dot{s} - c_\varphi s_\mu \dot{\xi} + c_\mu \dot{\varphi} \\ ((\tau c_\xi - \nu s_\xi)c_\varphi + \kappa s_\varphi)\dot{s} + s_\varphi \dot{\xi} + \dot{\mu} \\ ((\kappa c_\varphi + s_\varphi(\nu s_\xi - \tau c_\xi))c_\mu + s_\mu(\tau s_\xi + \nu c_\xi))\dot{s} + c_\varphi c_\mu \dot{\xi} + s_\mu \dot{\varphi} \end{bmatrix}. \quad (7)$$

The \dot{s} terms recognise the effect of the track curvatures on the angular velocity of the motorcycle body. As one would expect, these effects increase with vehicle speed. It is therefore necessary to describe the vehicle progress on the track as a function of the spine forward velocity \dot{s} . The velocities of the CoM $u = [u, v, w]^T$, in body-fixed frame B , are given by

$$\begin{aligned} \begin{bmatrix} u \\ v \\ w \end{bmatrix} &= R_y^T(\mu)R_x^T(\varphi)R_z^T(\xi)R_R^T \frac{d}{dt}(R_R R_z(\xi) R_x(\varphi) R_y(\mu)) \begin{bmatrix} 0 \\ y_r \\ -h \end{bmatrix} \\ &+ R_y^T(\mu) \left[R_x^T(\varphi)R_z^T(\xi)R_R^T \frac{d}{dt}(R_R R_z(\xi) R_x(\varphi)) \begin{bmatrix} 0 \\ 0 \\ z \end{bmatrix} + \begin{bmatrix} 0 \\ 0 \\ \dot{z} \end{bmatrix} \right. \\ &\quad \left. + R_x^T(\varphi)R_z^T(\xi) \begin{bmatrix} u_G \\ v_G \\ w_G \end{bmatrix} \right]. \end{aligned} \quad (8)$$

It is now possible to solve (7) and (8) for $[\dot{s}, \dot{n}, \dot{z}]^T$ and $[\dot{\xi}, \dot{\varphi}, \dot{\mu}]^T$ in order to obtain the kinematic transformations from the body-fixed frame variables and those in the spine frame. In particular, the \dot{s} equation allows the independent variable to be switched between the elapsed time and the elapsed distance travelled along the spine. This makes the optimal

control problem a fixed-horizon one. The differential equation for the elapsed distance is

$$\dot{s} = \frac{\left(((h\Omega_y + y_r\Omega_z + u) c_\mu + (w - y_r\Omega_x)s_\mu) c_\varphi + s_\varphi z (\Omega_x s_\mu - \Omega_z c_\mu) \right) c_\xi}{z c_\xi (c_\xi \tau - s_\xi \nu) - s_\varphi s_\xi n \nu + c_\varphi (1 - \kappa n)} - \frac{\left((c_\mu \Omega_x + \Omega_z s_\mu) z - h\Omega_x + v \right) s_\xi}{z c_\xi (c_\xi \tau - s_\xi \nu) - s_\varphi s_\xi n \nu + c_\varphi (1 - \kappa n)}. \quad (9)$$

The elapsed time is given by

$$J = \oint \frac{ds}{\dot{s}}, \quad (10)$$

which is the cost to be minimised. The closed-path integral corresponds to a lap of the circuit.

3.2. Vehicle dynamics

The accelerations of the CoM can be obtained from (7) and (8) by neglecting the (small) Darboux frame angular accelerations. The resulting expressions will be employed to compute the vehicle's EoMs using the Newton–Euler equations:

$$m\ddot{u} + m\omega \times u = F + mR_B^T g, \quad (11)$$

$$I\ddot{\omega} + \omega \times (I\omega) = M, \quad (12)$$

where m is the motorcycle mass, F and M are the vectors of external forces and torques on the motorcycle body, and $g = [0, 0, g]^T$ represents the acceleration due to gravity. By neglecting the effect of steering motions, the inertia tensor I in body-fixed reference frame is constant, and its roll–yaw inertia product is zero due to mid-plane symmetry. The (body-fixed) longitudinal EoM from (11) is

$$F_x = m \left(\dot{u} + v\omega_z + w\omega_y + g \left(c_\mu (\Theta c_\xi - \Phi s_\xi) + s_\mu (c_\varphi - s_\varphi (\Phi c_\xi + \Theta s_\xi)) \right) \right), \quad (13)$$

which has been linearised for small angles in $\delta, \delta_f, \Phi, \Theta$. The rotational EoMs are omitted due to their complexity. All the forces acting on the motorcycle in its body-fixed x -direction are denoted F_x . These include longitudinal tyre and aerodynamic influences. Tyre forces F_x^r, F_y^r, F_z^r , for the front and rear tyres, act at the contact points $P_{f,r}$. The aerodynamic drag F_D and lift F_L forces are applied at G , and are defined in the motorcycle's mid-plane (an aero pitching torque is also considered). As a consequence the vector F_x is given by

$$F_x = (F_x^r + F_x^f - F_y^f \delta_f - F_D) c_\mu + ((F_z^f + F_z^r) c_\varphi + (F_y^f + F_y^r - F_x^f \delta_f) s_\varphi - F_L) s_\mu. \quad (14)$$

The tyre forces are calculated using empirical magic formula [26]. As inputs, these formulae require the normal loads $F_z^{f,r}$, the longitudinal $\kappa_{f,r}$ and lateral $\alpha_{f,r}$ slips, and the tyre camber angles with respect to road plane φ_f, φ . The slips and camber angles can be calculated using kinematic relationships such as (3). The tyre normal loads are calculated by means of the

lumped spring-dampers relationships

$$\begin{aligned} F_z^f &= \frac{k_t^f}{\cos(\varphi_f)^2} \zeta_f + c_t \dot{\zeta}_f, \\ F_z^r &= \frac{k_t^r}{\cos(\varphi)^2} \zeta_r + c_t \dot{\zeta}_r, \end{aligned} \quad (15)$$

whose associated stiffnesses $k_t^{f,r}$ represent the radial deformation of the tyres. The tyre carcass damping constant is c_t . Tyre aligning and overturning moments are given by the moment arm of tyre forces with respect to the wheel hubs; rolling resistance is neglected.

The aerodynamic coefficients $C_{D,L}$ are adjusted for a prone and standing rider, which accounts for the rider motion during acceleration and braking manoeuvres. In the aerodynamic model given below, a hyperbolic tangent function, whose slope is set by parameter A , is used to provide a smooth transition between prone and standing rider configurations:

$$\begin{aligned} F_{D,L} &= \frac{1}{2} \rho C_{D,L} u_G^2, \\ C_{D,L} &= C_{D,L}^p - (C_{D,L}^s - C_{D,L}^p) \frac{\tanh(A\kappa_f)}{2}. \end{aligned} \quad (16)$$

The rider will be standing under braking ($\kappa_f < 0$), and in this case the ‘*s*’ variants of the aerodynamic coefficients will be adopted. Otherwise the prone ‘*p*’ parameters will be used.

Steering dynamics are included in the model by adding another (second order) differential equation to (11) and (12), which represents the influence of changes in the steering angle δ . The additional equation can be found using either a Newton–Euler or Lagrange approach. In the second case one would use

$$\frac{d}{dt} \left(\frac{\partial \mathcal{L}}{\partial \dot{\delta}} \right) + \frac{\partial \mathcal{L}}{\partial \delta} = M_\delta - c_\delta \dot{\delta} \quad (17)$$

in which \mathcal{L} is the Lagrangian function associated with the front assembly rotation around the steer axis. The steering control torque is M_δ , with $c_\delta \dot{\delta}$ representing the steering damper torque which acts on the steered assembly and reacts on the vehicle’s main body. Gyroscopic effects due to wheel rotations are introduced by adding two further differential equations that describe the wheel angular velocities $\omega_{f,r}$. In order to keep the model simple enough to be compatible with optimal control solvers, the fast dynamics of the drive train is not included in the model. The system of equations (11), (12) and (17) have a constant mass matrix (once steering motion is neglected), which is easily inverted either symbolically or numerically. The EoMs, originally derived with time as the independent variable, are transformed so that elapsed distance along the spine is the independent variable, by multiplying the right-hand sides by $1/s$ using (9).

4. Optimal control

A broad outline of the vehicular optimal control can be found in [8,11], with a more detailed discussion of the various numerical methods in [9,21]. We will only provide a brief summary here, focussing on the control issues specific to motorcycle control.

The minimum-lap-time optimal control problem is solved using GPOPS-II [16], which is a direct pseudospectral method based on Legendre–Gauss–Radau collocation and Radau’s integration formula. The solution is found by iteratively minimising the discrete approximation of the cost function in (10), which is constrained by the track boundaries and the vehicle’s equations of motion. In sum, the performance index together with the equations of motion, the boundary, input and state constraints is converted into a large sparse nonlinear programme (NLP). A gradient descent based optimisation algorithm (such as SNOPT or IPOPT [27]) is used to solve the resulting NLP. The first- and second-order partial derivatives associated with the cost, the path constraints, and the system dynamics must be given to the solver. Since analytical expressions are available for the above quantities, it is straightforward to symbolically compute the derivatives with respect to the states and controls. In the work presented here, the requisite Jacobians and Hessians are computed using an algorithmic differentiation algorithm [28].

To assist the convergence of the NLP solver, the problem is scaled in order to bring the decision variables into a ‘more spherical’ hyperspace. To do this the fundamental quantities including mass, length and time were normalised with respect to the motorcycle’s mass m and wheelbase w respectively, while time is scaled according to $\sqrt{g/w}$ [21]. With the vehicle parameters reported in Appendix, a lap-time of 110 s becomes 281, the normal tyre load of 2500 N becomes 1.02, and a top speed of 100 m/s becomes 26 in a dimensionless framework. All angle-related quantities are unscaled.

In an important class of optimal control problems the system equations and the performance index are linear functions of the control variables. This situation occurs, for example, in minimum-time problems. Indeed, when a given distance needs to be traversed in minimum time, the longitudinal control input doesn’t appear in the cost function, while it appears linearly in the equations of motion [21]. When Pontryagin’s Maximum Principle (PMP) is used to determine the optimal controls for this type of problem, the solution takes the general form

$$u^*(t) = \begin{cases} a & \text{if } \Gamma(t) < 0, \\ \text{unknown} & \text{if } \Gamma(t) = 0, \\ b & \text{if } \Gamma(t) > 0, \end{cases} \quad (18)$$

where a and b are, respectively, upper and lower bounds on the admissible control $u(t)$. The switching function $\Gamma(t)$ is a collection of the coefficients of the control terms in the control Hamiltonian. Controls that switch between the upper and lower control limits are called *bang–bang* controls. In some problems the switching function $\Gamma(t)$ is singular over a finite time interval. During this interval, the Hamiltonian function is no longer an explicit function of the controls u and the PMP yields no information about the optimal control. This is when singular arcs occur.

A way to avoid the singular arc phenomenon is to introduce into the performance index regularising terms that are quadratic in the controls, which are small enough not to distort the solution to the original problem. That is

$$J_{reg} = \oint \frac{1}{s} \left(1 + \sum_{i=1}^{N_u} \epsilon_i u_i^2 \right) ds. \quad (19)$$

The weighting factors ϵ_i must be as small as possible, while achieving a reliable solution. It has been shown in the car case [11] that the perturbation on the solution introduced by regularisation terms is comparable to that introduced by different mesh refinement strategies, and is approximately 0.1% of the true minimum time computed by (10).

4.1. Motorcycle OCP setup

Motorcycle optimal control has a number of unique features that we will now summarise. When accelerating firmly, mainly in straight running, motorcycles can have a ‘light’ front wheel (wheelie) that renders the vehicle’s steering ineffective. In a similar way, under firm front wheel braking, the rear wheel can leave the road (stoppie). Under these conditions, the rear/engine brake can do little more than reduce the angular momentum of the rear wheel. As one would expect, the optimal control solver will seek to avoid these debilitating operating regimes. Also, in order to maintain faith with the physics, the tyre normal loads must be restricted so that $F_z^{f,r} \leq 0$; forces of attraction between the tyre and road cannot be allowed. In the same way, driving torques cannot be allowed on the front wheel. From a purely kinematic perspective, the vehicles roll angle must be restricted to something of the order $|\varphi| \leq 65^\circ$. Cossalter et al.[12] introduced quadratic terms on the controls in the cost function as a measure of vehicle manoeuvrability. For example, the integrated rate of change of steering torque \dot{M}_δ , can be viewed as a cost of the actuation. This quantity is also loosely related to the vehicle’s handling. The same ideas are used here in order to obtain control time histories that are representative of human rider behaviour. These include limited control bandwidth, maximum steering torque, and limited peak roll rates.

Assembling these ideas, together with longitudinal control regularisation terms, leads to the cost function used in this study:

$$J_{reg} = \oint \frac{1}{s} \left(1 + (\epsilon_1 + \epsilon_2 \dot{\varphi}^2) \dot{M}_\delta^2 + \epsilon_3 \dot{\kappa}_r^2 + \epsilon_4 \dot{\kappa}_f^2 \right) ds. \quad (20)$$

Table 1. Motorcycle OCP structure.

		Description
	Integrated states	
1,2,3	u, v, w	Motorcycle CoM velocities (Equation (11))
4,5,6	s, n, z	Motorcycle CoM positions (Equation (8))
7,8,9	$\omega_x, \omega_y, \omega_z$	Motorcycle body angular velocities (Equation (12))
10,11,12	φ, μ, ξ	Motorcycle body orientation (Equation (7))
13,14	$\delta, \dot{\delta}$	Steering velocity and position (Equation (17))
15,16	κ_f, κ_r	Longitudinal slips
17	M_δ	Steering torque
	Controls	
1,2	$\dot{\kappa}_f, \dot{\kappa}_r$	Longitudinal slip rates
3	\dot{M}_δ	Steering torque rate
	Path constraints	
1,2	$F_z^f < 0, F_z^r < 0$	Unilateral wheel ground contact force
3	$F_x^r(1 + \kappa_r)u_G \leq P_{max}$	Max power constraint
4,5	$P_{f,r} \geq n_l$	Left track boundaries constraint
6,7	$P_{f,r} \leq n_r$	Right track boundaries constraint

The roll-rate dependent term in the steering torque regularisation is used to reduce the peak steering torque in chicane manoeuvres to realistic values. The weighting factors $\epsilon_{1,2}$ were ‘tuned’ to experimental data as will be explained in Section 5.1.2. The objective function (20) produced a smoother control behaviour than (19). This change also resulted in a coarser mesh, and an average reduction in computation time of 20% is thus observed. The tyre slip rates $\dot{\kappa}_{f,r}$ were chosen as the control inputs, and box bounds were used to ensure that only braking force can be exerted by the front tyre. The maximum rear tyre force was limited to reflect the engine power available at the rear wheel by the inequality constraint $F_x^r(1 + \kappa_r)u_G \leq P_{max}$. Finally, the positions of the tyre contact points were constrained to remain within the track boundaries. A summary of the optimal control problem parameters is given in Table 1. Cyclic constraint is imposed on all the states and controls, so that the (free) first and last points of the computed lap coincide.

5. Simulation results

5.1. Validation with experimental data

In order to validate the model and the modelling assumptions relating to the optimal control problem, a comparison was made between simulation results on a 3D track model and telemetry data. The vehicle used is representative of a 1000 cc, 4-stroke, production race motorcycle (World Superbike class). The data was acquired by an inertial measurements unit (three orthogonal accelerometers, and three orthogonal rate gyros), with suspension and steering angle position sensors. The test was conducted in a private test session, with a professional rider, in ideal conditions (dry track, moderate temperature and no wind). The machine was fitted with qualifying tyres. The vehicle states were estimated from measurement data using an Extended Kalman Filter [29]. The data from the best lap of the session is used in order to get as close as possible to the edge of the performance envelope of the vehicle. Since the longitudinal and lateral tyre peak friction coefficients are unknown, they were adjusted in order that the simulation results match the test results in terms of lap time, maximum roll angle, and mid-corner speed. In particular, the MF scaling factors for longitudinal and lateral tyre grip $\lambda_{\mu,x}$ and $\lambda_{\mu,y}$ of the rear tyre have been altered to acknowledge the different operating temperature and asphalt roughness of the actual racetrack wrt the tyre testing facility. The aerodynamic force coefficients, as well as rider movement maps, were identified for the particular test rider.

Figure 5, top two panels, shows the measured and simulated speed and roll angle profiles. The independent variable is the distance travelled along the racing line s_{rl} – the measured and predicted lap times differs by 0.18 s, with a total lap time of over 110 s. The measured lap distance travelled is 5178 m, while that for a simulated lap is 5174 m. Some of the data has been anonymised for commercial reasons, particularly parameters relating to the tyre-vehicle combination. The longitudinal velocity u_G , the roll angle φ and roll rate $\dot{\varphi}$, and the longitudinal and lateral accelerations \ddot{u} , \ddot{i} , have been normalised with respect to their maximum values. The same scaling process is applied to the tyre forces $F_x^{f,r}$ and $F_y^{f,r}$, and the associated friction coefficients $\mu_{x,y}^{f,r} = F_{x,y}^{f,r}/F_z^{f,r}$.

The third panel in Figure 5 shows the computed optimal racing line curvature, which is compared to the racing line curvature chosen by the rider. The computed and measured steering angles are shown at the bottom of the same figure. The race line curvature is the

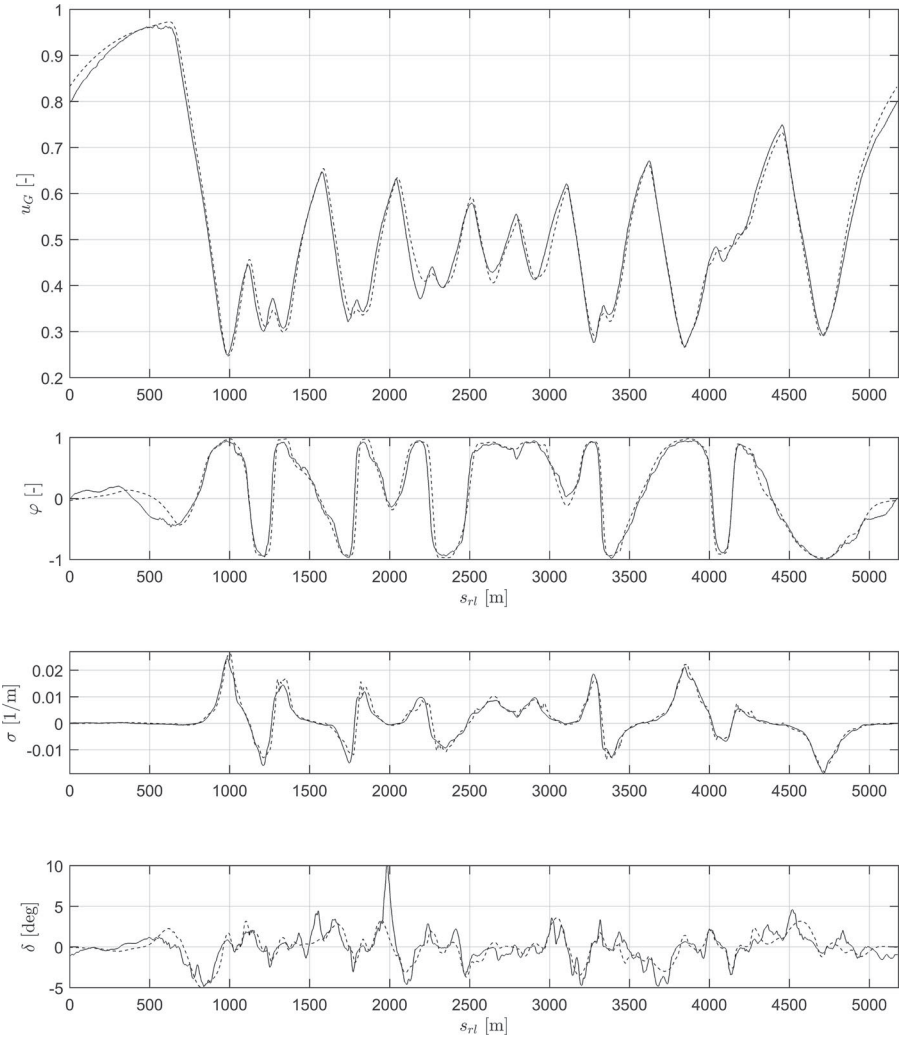


Figure 5. Velocity, roll angle, racing line curvature and steer angle profiles as a function of elapsed racing-line distance from the start–finish line for the Mugello racetrack. Solid line: experimental, dashed line: simulation.

ratio of the acceleration of G normal to the racing line, and the square of the vehicle speed:

$$\sigma = \frac{\dot{v}_G \cos \beta - \dot{u}_G \sin \beta}{u_G^2 + v_G^2}, \quad (21)$$

where $\beta = \arctan(v_G/u_G)$ is the motorcycle's mid-plane heading angle with respect to the (optimal) racing line. In the SAE sign convention, the roll angle, the steer angle and the track curvature are positive for right-hand corners. Apart from a 'spike' in the steering angle at approximately 2000 m, the agreement between the measured and computed results is again excellent. The spurious spike is the result of a momentary loss of control by the rider when approaching the braking point for corner 6.

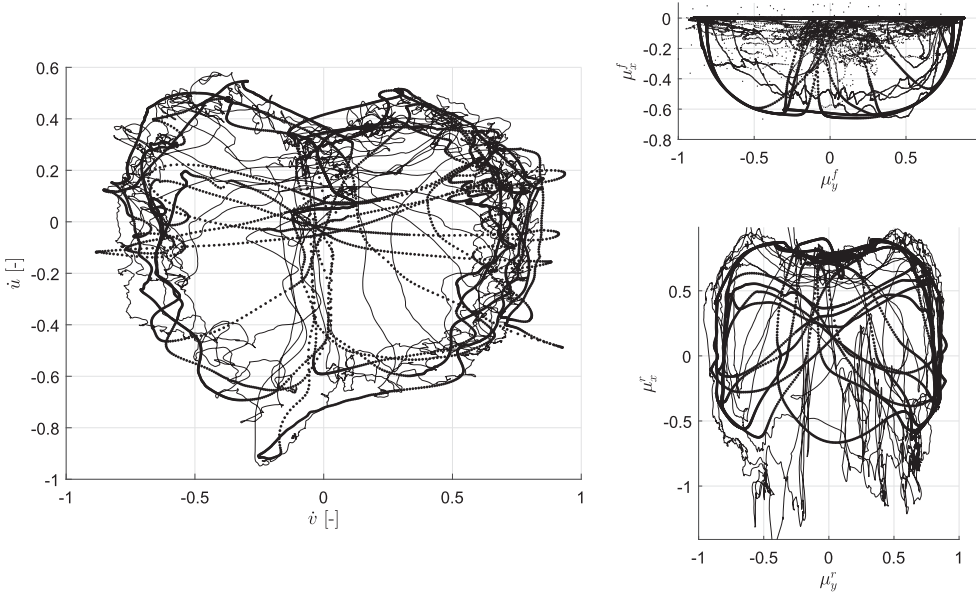


Figure 6. G-G diagram, and rear and front tyre adherence coefficients. Thin line: experimental, dots: simulation.

Figure 6 provides G-G diagram type performance summary (for the CoM) along with the lateral and longitudinal friction coefficients ($\mu_x - \mu_y$) of each tyre.

Since a magic formula type tyre models is adopted, the friction envelope is not ellipsoidal. The front tyre operates in the lower half of the friction characteristic, because this wheel is undriven. A clear indentation is evident in the upper half of the rear tyre friction characteristic due to the ‘wheelie’ limit that comes into play during acceleration out of corners at low roll angles. The simulation results again show very good agreement with the measured data.

5.1.1. U-turn manoeuvre

A detailed analysis of the left-handed U-turn corner 15 is given next; see Figure 1. The computed optimal trajectory is presented in Figure 7, which demonstrates the well known ‘wide-in wide-out’ behaviour, making use of the entire width of the track in order to maximise the turn’s radius of curvature. The minimum velocity is found, as expected, at the point of maximum roll angle in correspondence with the peak racing line curvature at 4715 m; the correlation with the telemetry is excellent. By following the tyre grip usage along the manoeuvre (Figure 8), it is clear that the rider brakes sharply at 4460 m with both tyres. At this moment almost all the motorcycle and rider weight is on the front tyre (see the simulated vertical load F_z in Figure 8). The rider then releases the brakes, while staying on the edge of the front-tyre adhesion envelope. He then accelerates again using the full rear tyre combined slip capacity with the vehicle’s entire weight on the rear tyre (the wheelie limit). In sum, the factors limiting the vehicle’s performance in the U-turn manoeuvre are as follows: from approx. 4520 to 4640 m both tyres are saturated (maximum braking and lateral adherence capabilities are employed). From approx. 4640 to 4760 m the front tyre

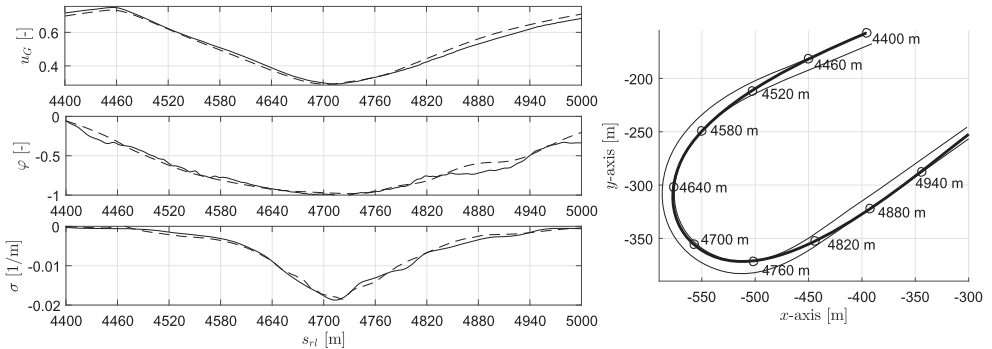


Figure 7. Corner 15: speed, roll angle, curvature and racing line. Solid line: experimental, dashed line: simulation.

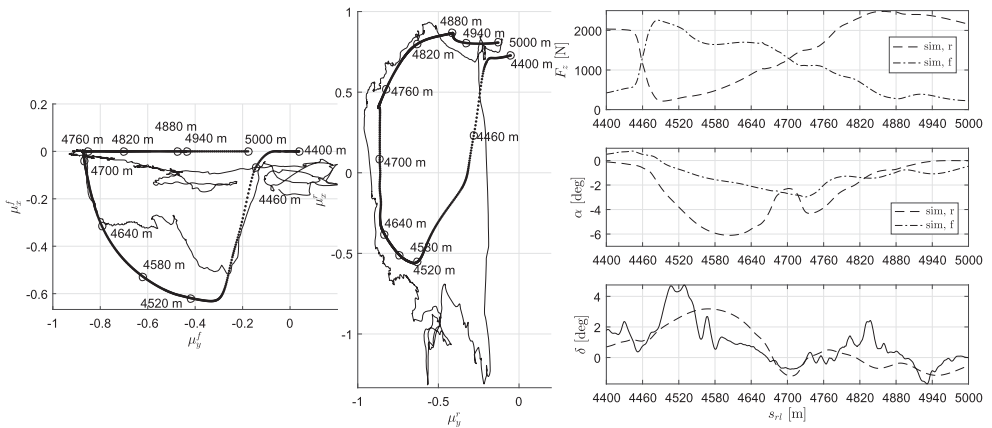


Figure 8. Vehicle behaviour for Corner 15 (thin line: experimental, dots: simulation). The front and rear tyre usage, respectively, is shown on the left and centre plots. On the right are the vertical loads, the tyre slip angles (dashed line: simulation rear, dash-dot line: simulation front) and the steer angle (solid line: experimental, dashed line: simulation).

is saturated (from 4700 m in pure lateral saturation). From approx. 4760 to 4880 m, under acceleration at high roll angle, the rear tyre is saturated in combined lateral and longitudinal slip. From 4880 m front tyre leaves the road surface.

A possibly novel insight into the U-turn manoeuvre can be drawn from the vehicle's attitude throughout the manoeuvre. During the turn-in phase both tyres are saturated, predominantly under braking, with the rear tyre slip angle substantially higher than that of the front tyre due to the low vertical load on the rear tyre; see F_z and α in Figure 8. The manoeuvre gives the vehicle a 'nose-in' attitude pointing to the apex of the corner. This requires corrective counter steering as is evident from the steer angle plot (δ) plot in Figure 8 (steering to the left is negative). During the front tyre saturation phase (starting at 4700 m), the front tyre slip angle necessarily increases, becoming larger than that of the rear tyre. As a consequence the vehicle assumes a 'nose-out' posture, with the steering assembly turned into the corner, hitting the apex (at 4715 m). During the subsequent acceleration out of the

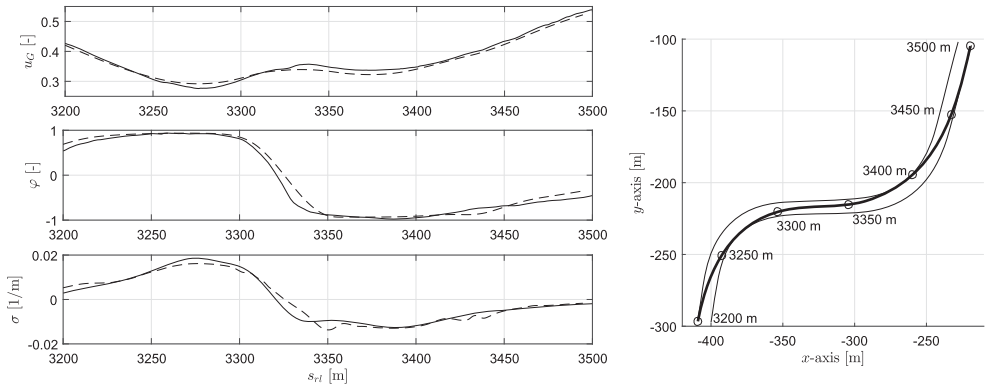


Figure 9. Corners 10–11: speed, roll angle, and racing-line curvature. Solid line: experimental, dashed line: simulation.

corner, the rear tyre exhibits a larger slip angle giving the vehicle a ‘nose-in’ posture that gradually decays towards the straight. By comparing the simulated and measured steering angle, it is evident that the magic formula tyre model is able to capture this behaviour precisely, providing valuable insight into the cornering strategies of professional riders.

5.1.2. Chicane manoeuvre

The right-left corners 10 and 11 are used as an example of the chicane manoeuvre; see Figure 1. The trajectory into turn 10 closely resembles that used in the U-turn manoeuvre: firm front and rear braking is used with the vehicle assuming a ‘nose-in’ posture corrected by counter steering. Under these conditions, both tyres are on the saturation limit up to the apex at approximately 3290 m; this is followed by a brief acceleration phase at 3300 m see Figure 9. At 3330 m, approximately 40 m after first corner apex, the motorcycle is flipped from side to side (see roll angle φ in Figure 9 and the roll rate $\dot{\varphi}$ in Figure 10), in order to turn into corner 11. Here the performance limiting factor is the handlebar torque required from the rider. As is well known, the front wheel gyroscopic moment, combined with a high roll rate, makes for a high steering torque requirement. Limiting the roll rate in the cost function (20) makes it possible to limit the handlebar torque to realistic values. This restriction also has the effect of ‘smoothing out’ the roll-rate profile. Indeed, simple box-bounds on the steering torque would result in a bang-bang actuation of the steering, which is practically unrealistic. Once the turn-in braking phase is complete, both corners are traversed laterally saturating both tyres; in particular, the front tyre switches from pure right-side lateral slipping when apexing turn 10, to pure left-side lateral slipping when apexing turn 11. Since the track curvature reduces after both turns, front tyre saturation occurs only briefly. During this manoeuvre the posture of the vehicle at each chicane apex is neutral (as opposed to the ‘nose-out’ posture assumed in the U-turn); approximately the same slip angles are used on the front and rear tyres, with only minimal steering correction.

5.2. Comparison between 2D and 3D track profiles

There are three significant effects that influence the performance of a motorcycle on a 3D track. The first is the varying orientation of the vehicle relative to gravity, the second is

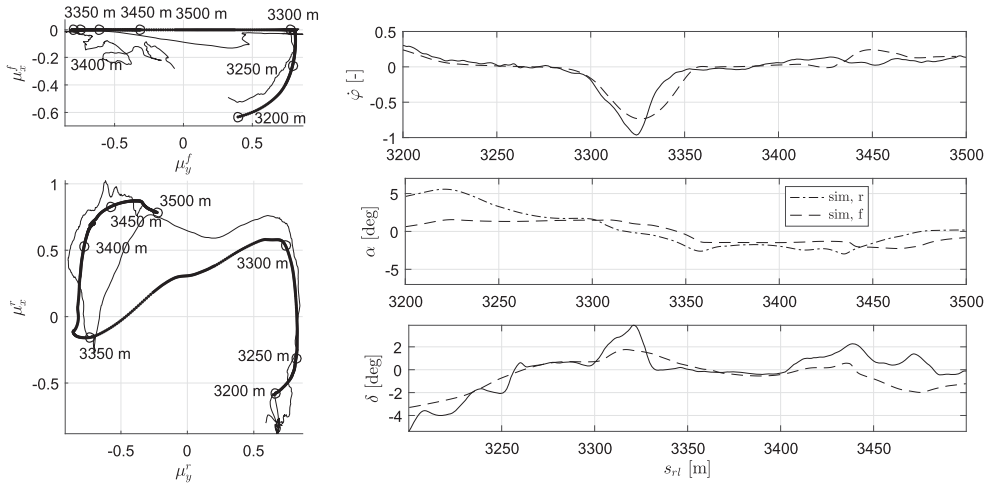


Figure 10. Corners 10 and 11: tyre grip usage (thin line: experimental, dots: simulation). The right-hand side of the figure shows the roll rate (solid line: experimental, dashed line: simulation), the tyre slip angles, and the steering angle (solid line: experimental, dashed line: simulation).

variations in track camber, and the third is centripetal forces resulting from the vehicle driving at speed over varying road inclinations (dips and the crests of hills). To highlight these effects on the optimal lap, the simulations from the previous section are compared to those for a ‘flat track’ model. A flat track is achieved by setting the track’s relative torsion and normal curvature (respectively Ω_x and Ω_y), as well as the associated Euler angles (Φ and Θ respectively) to zero. These comparisons are made in Figure 11. The top plot (in Figure 11) shows that the lap time in the 2D case is 5% longer; the removal of 3D influences reduces the full-lap ridden distance from 5174 to 5172 m. It is evident that time is lost, mid-corner, in the 2D case, in turns 1, 8, 9, 12, 15 due to the absence of positive road camber. However, the time gained in turn 9 is offset by the uphill road gradient, as will be highlighted in Section 5.2.2. The time difference plot shows how each of the five corners account for more than 2.8 s of the total 4.5 s lap-time difference. The second (from the top) panel shows that the motorcycle roll angle is unaffected by road cambering; the reason for this will be explained in Section 5.2.1. The third panel shows that the normal load variations $F_z^{tot} = F_z^f + F_z^r$ are attributable mainly to centripetal force in the vertical direction due to road elevation changes. These normal load variations can be approximated by $\Delta F_z^{tot} \approx m(u_G \Omega_y) = m(u_G \tau \dot{s})$. The effect of the crest on the main straight (at approximately 500 m) is evident. The fluctuations thereafter amount to approximately 20% of the vehicle’s weight. Also, the blind crests before the braking points for corners 10 and 12, are approached with reduced normal tyre loads.

5.2.1. Road camber influences

Several insights into the influence of road cambering on motorcycle dynamics can be obtained by studying the vehicle’s cornering equilibrium on a cambered road, see [21]. The machine is subjected to gravitational, centripetal, and vertical and lateral tyre forces. It is straight forward to write down the steady-state equilibrium equations for constant-speed

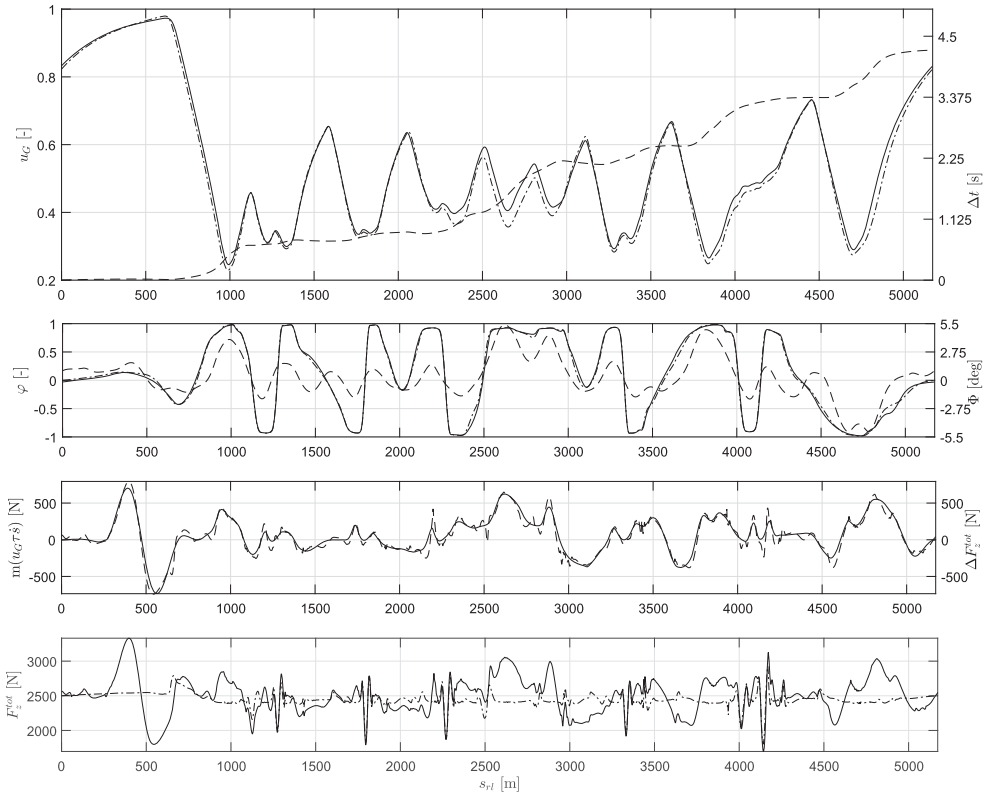


Figure 11. Comparison between a 2D and 3D track. Top plot: speed (the 2D case is shown dash-dot, while the 3D case is shown solid), and the lap-time difference Δt ; second plot: roll angle and road camber angle; third plot: road pitch rate induced vertical force and total vertical ground force difference; and fourth plot: total vertical ground force F_z^{tot} . The right-hand axis plots are shown (dashed).

cornering in presence of road camber angle Φ , if we treat the motorcycle and rider as a point mass m located at the CoM. Balancing lateral and vertical loads, and taking moments around the contact point gives

$$\begin{aligned} F_y^{tot} &= m(g \sin \Phi - u^2 \sigma \cos \Phi), \\ F_z^{tot} &= m(g \cos \Phi + u^2 \sigma \sin \Phi), \\ h_G \tan(\varphi) &= \frac{u^2 \sigma \cos \Phi - g \sin \Phi}{u^2 \sigma \sin \Phi + g \cos \Phi}. \end{aligned} \quad (22)$$

As in the motorcar case [11], positive cambering increases the vertical tyre loads, while at the same time requiring reduced lateral tyre force to balance the centripetal load. The roll equilibrium equation, on the other hand, shows how a reduced roll angle is required to achieve a moment balance when road cambering is introduced.

These three effects, along with the pitch-rate induced increases in vertical load, explain the performance differences in the corners featuring cambering such as turns 1, 8, 9, 12, 15. As an example, the 2D-vs-3D road simulations for corner 1 are illustrated in Figure 12. It is evident that the total vertical tyre load F_z^{tot} and the lateral tyre force F_y^{tot} are both increased,

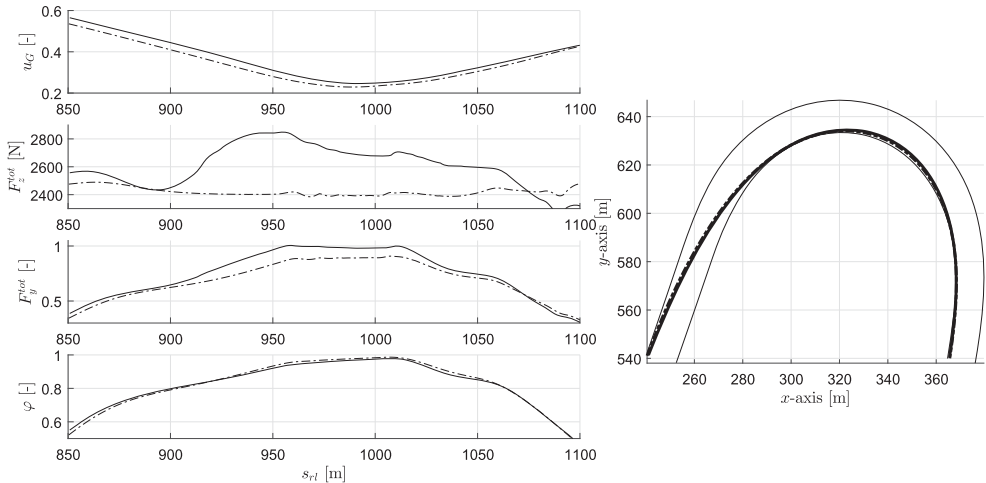


Figure 12. Corner 1: speed profile, total vertical and lateral ground forces, and roll angle; the 2D case is shown dash-dot, while the 3D case is shown solid.

while the roll angle φ remains substantially the same. The increased lateral tyre force comes from increased speed. The roll angle (with respect to the road) is almost unchanged. As a consequence, the tyres are operated at almost the same (optimal) working point (small differences may be introduced by adhesion dependencies on the normal tyre load). That said, the vehicle's roll angle is increased with respect to the inertial reference system, making it possible to accommodate a higher centripetal load. The optimal racing line is slightly wider when road banking is introduced, with the speed increase more than compensating for the longer route through the corner.

5.2.2. Road pitching influences

Assuming a point mass model in the longitudinal direction, a corresponding force balance is given by

$$m\dot{u} = F_D - F_A - mg \sin \Theta$$

in which F_D and F_A are the drive and aerodynamic drag forces respectively. The final part of the straight uphill stretch following corner 9 is shown in Figure 13 (see also the elevation profile in Figures 2 and 1). Starting at the apex of turn 9, a road-camber related speed difference is evident; this was discussed in Section 5.2.1. This figure also provides evidence of the retarding influence of the uphill gradient, which is roughly comparable to that associated with the aerodynamic drag. By the time vehicle reaches 2975 m, the mid-corner speed advantage has been cancelled by the uphill road gradient. Despite the 5 km/h speed advantage gained on the exit of turn 9 (relative to the 2D case), the motorcycle reaches the braking point into turn 10 approximately 4 km/h slower. The combined effects of road camber and pitch, and vertical and lateral centripetal forces are evident in corners 7 and 8, where the optimal control takes advantage of the track topology by altering the racing line. See Figure 14. As a result of the road pitching and the associated vertical centripetal force, the speed through corner 7 is approximately 8 km/h higher in the 3D case (see Figure 1). At the corner exit, a higher lateral centripetal force is experienced, due to both the higher

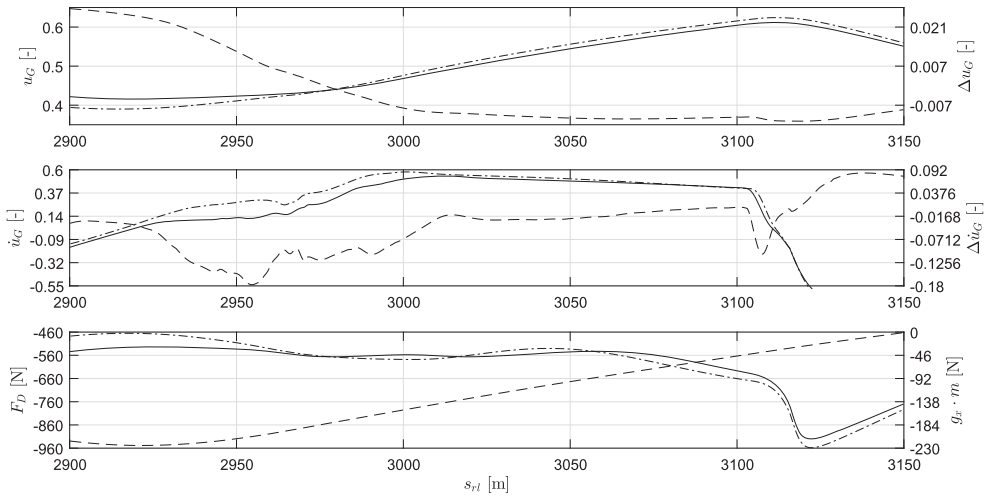


Figure 13. Corner 9: speed profile, longitudinal acceleration, gravitational and aerodynamic drag forces; the 2D case is shown dash-dot, while the 3D case is shown solid. The right-hand axis quantities are shown dashed.

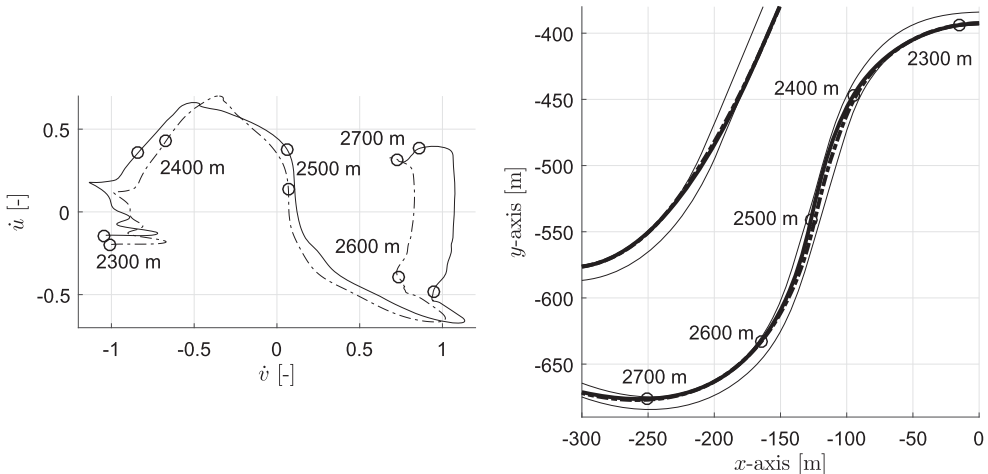


Figure 14. Corners 7 and 8: G-G diagram and optimal racing line; 2D track (dash-dot), and 3D track (solid).

speed through the corner and the road camber rate effect induced by the road camber sign change between corners 7 and 8. As a consequence, the vehicle runs wider out of the corner, and a wider line connecting the corners is chosen. This means that the entry line into corner 8 is tighter in the 3D case. Due to the rapid variation in road pitch from the down-hill section approaching corner 8, to following uphill section, as well as the positive road camber, the substantial speed difference (more than 10 km/h) between 2D and 3D track is found at this corner; see Figure 11. Despite a tighter line into turn 8, and a slightly tighter line at corner exit, 3D effects make it possible to increase simultaneously the speed and curvature of the resulting (shorter) racing line.

6. Conclusions

The primary aim of this work was to validate dynamic minimum-lap-time optimal control simulations for a sports motorcycle on a 3D track. Measured data were obtained from an instrumented motorcycle ridden by a professional rider in a private test session. This study is a natural extension of parallel research that was conducted for a Formula One car driven on a 3D track.

The motorcycle model used in this study is a modified version of the classical Whipple bicycle, which is shown to accurately represent the basic motions of the vehicle. These motions include the vehicle's steering and roll angle behaviour, contributions from track camber and elevation changes, and the vehicle's sprung mass motion relative to the track.

Important features of the model include its ability to describe all the performance limiting factors of the vehicle such as front and rear roll-over, tyre adhesion (via magic formulae), and the engine power in a concise form. In studies of this type, it is important to find a model that is both sufficiently accurate, and a suitable part of an optimal control problem solver. We used direct collocation and an open-source NLP solver, as well as automatic differentiation, thereby removing the need to derive co-state equations and system derivatives.

A regularisation process was used to represent accurately the steering torque and power limits associated with a rider's ability to ride the motorcycle at racing speeds. Unusually, the theoretical simulation work has been successfully validated against measured data on the Mugello race track. A comparison between measured and predicted data highlights how the proposed vehicle model makes it possible to predict the directional behaviour of the vehicle, in a minimum-time manoeuvring framework, providing novel insight into the riding style of top-level racing riders on high-power motorcycles.

The influence of the 3D track on the optimal performance of the vehicle was also analysed. It was found that the most important influences on the lap time were: (i) the vertical road pitch rate induced centripetal forces, which provide additional down forces, which can broaden or restrict the vehicle's performance envelope, and (ii) the road banking that makes it possible to support higher cornering speeds without exceeding the roll angle limits of the vehicle, or the camber force limits of the tyres.

A further development of the work presented would be the inclusion of suspension dynamics in the vehicle model. This will allow for a better description of the motorcycle kinematics in terms of CoM height, wheelbase and weight distribution, improving the accuracy of the simulation during the front and rear wheelie phases through the lap. Another important investigation would be the inclusion of tyre temperature and wear dependence in the model, extending the work that has been carried out for racing cars in [30].

Disclosure statement

No potential conflict of interest was reported by the authors.

References

- [1] Scherenberg H. Mercedes-benz racing design and cars experience. SAE Trans. 1958;66(580042): 414–420.
- [2] Milliken DL, Milliken WF. Race car vehicle dynamics: problems, answers, and experiments. Warrendale (PA): SAE International; 2003.

- [3] Brayshaw D, Harrison M. A quasi steady state approach to race car lap simulation in order to understand the effects of racing line and centre of gravity location. *Proc Inst Mech Engineers Part D – J Autom Eng.* **2005**;219:725–739.
- [4] Hendrikx JM, Meijlink T, Kriens RFC. Application of optimal control theory to inverse simulation of car handling. *Veh Syst Dyn.* **1996**;26(6):449–461.
- [5] Casanova D. On minimum time vehicle manoeuvring: the theoretical optimal lap [dissertation]. Bedford: Cranfield University, School of Engineering; 2000.
- [6] Rucco A, Notarstefano G, Hauser J. An efficient minimum-time trajectory generation strategy for two-track car vehicles. *IEEE Trans Control Syst Technol.* **2015**;23(4):1505–1519.
- [7] Rucco A, Notarstefano G, Hauser J. Development and numerical validation of a reduced-order two-track car model. *Eur J Control.* **2014**;20(4):163–171.
- [8] Perantoni G, Limebeer DJN. Optimal control for a formula one car with variable parameters. *Veh Syst Dyn.* **2014**;52(5):653–678.
- [9] Limebeer DJN, Rao AV. Faster, higher, and greener: vehicular optimal control. *IEEE Control Syst.* **2015**;35(2):36–56.
- [10] Perantoni G, Limebeer DJN. Optimal control of a formula one car on a three-dimensional track – part 1: track modeling and identification. *J Dyn Syst Meas Control.* **2015**;137:051018.
- [11] Limebeer DJN, Perantoni G. Optimal control of a formula one car on a three-dimensional track – part 2: optimal control. *J Dyn Syst Meas Control.* **2015**;137:051019.
- [12] Cossalter V, Da Lio M, Lot R, et al. A general method for the evaluation of vehicle manoeuvrability with special emphasis on motorcycles. *Veh Syst Dyn.* **1999**;31:113–135.
- [13] Lot R, Massaro M. A symbolic approach to the multibody modeling of road vehicles. *Int J Appl Mech.* **2017**;9(5):1750068.
- [14] Bertolazzi E, Biral F, Da Lio M. Symbolic-numeric efficient solution of optimal control problems for multibody systems. *J Comput Appl Math.* **2006**;185(2):404–421.
- [15] Van Wyk EJ, Falugi P, Kerrigan EC. ICLOCS. 2010. Available from: <http://www.ee.ic.ac.uk/ICLOCS>
- [16] Patterson MA, Rao AV. GPOPS-II: a matlab software for solving multiple-phase optimal control problems using hp-adaptive Gaussian quadrature collocation methods and sparse nonlinear programming. *ACM Trans Math Softw.* **2014**;41(1):1. doi:10.1145/2558904
- [17] Massaro M, Marconi E. The effect of engine spin direction on the dynamics of powered two wheelers. *Veh Syst Dyn.* **2018**;56(4):604–620.
- [18] Bobbo S, Cossalter V, Massaro M, et al. Application of the optimal maneuver method for enhancing racing motorcycle performance. *SAE Int J Passenger Cars – Mech Syst.* **2009**;1(1):1311–1318.
- [19] Hauser J, Saccon A. Motorcycle modeling for high-performance maneuvering. *IEEE Control Syst.* **2006**;26(5):89–105.
- [20] Evangelou S, Tomas-Rodriguez M. Influence of road camber on motorcycle stability. 2008 3rd International Symposium on Communications, Control and Signal Processing; vol. 3; 2008. p. 231–236.
- [21] Limebeer DJN, Massaro M. Dynamics and optimal control of road vehicles. Oxford: Oxford University Press; **2018**.
- [22] Snyder JP. Map projections: a working manual. U.S. Government Printing Office; 1987.
- [23] Whipple F. The stability of the motion of a bicycle. *Quart J Pure Appl Math.* **1899**;30: 312–348.
- [24] Meijaard J, Papadopoulos JM, Ruina A, et al. Linearized dynamics equations for the balance and steer of a bicycle: a benchmark and review. *Proc R Soc Lond A: Math Phys Eng Sci.* **2007**;463(2084):1955–1982. Available from: <http://rspa.royalsocietypublishing.org/content/463/2084/1955>
- [25] Basu-Mandal P, Chatterjee A, Papadopoulos J. Hands-free circular motions of a benchmark bicycle. *Proc Roy Soc Lond A: Math Phys Eng Sci.* **2007**;463(2084):1983–2003. Available from: <http://rspa.royalsocietypublishing.org/content/463/2084/1983>
- [26] Pacejka HB. Tyre and vehicle dynamics. Oxford: Butterworth-Heinemann; **2012**.

- [27] Wächter A, Biegler LT. On the implementation of a primal–dual interior point filter line search algorithm for large-scale nonlinear programming. *Math Program.* **2006**;106(1): 25–57.
- [28] Weinstein MJ, Rao AV. Algorithm 984: adigator, a toolbox for the algorithmic differentiation of mathematical functions in matlab using source transformation via operator overloading. *ACM Trans Math Softw.* **2017**;44(2):21. doi:10.1145/3104990
- [29] Teerhuis AP, Jansen ST. Motorcycle state estimation for lateral dynamics. *Veh Syst Dyn.* **2012**;50(8):1261–1276.
- [30] Tremlett AJ, Limebeer DJN. Optimal tyre usage on a formula one car. *Veh Syst Dyn.* **2016**;54(10):1448–1473.

Appendix. Motorcycle model parameters

Motorcycle geometry

Wheelbase	$w = 1.5 \text{ m}$
Height of the CoM	$h = 0.6 \text{ m}$
Longitudinal position of CoM	$b = 0.73 \text{ m}$
Caster angle	$\mu_0 = 0.45 \text{ rad}$
Normal trail	$t_n = 0.1 \text{ m}$
Rear tyre un-deformed radius	$R_r = 0.33 \text{ m}$
Rear tyre torus radius	$\rho_r = 0.1 \text{ m}$
Front tyre un-deformed radius	$R_f = 0.3 \text{ m}$
Front tyre torus radius	$\rho_f = 0.06 \text{ m}$

Inertial properties

Motorcycle and rider mass	$m = 250 \text{ kg}$
Front assembly mass	$m_f = 30 \text{ kg}$
Motorcycle roll inertia	$I_{xx} = 18 \text{ kg m}^2$
Motorcycle pitch inertia	$I_{yy} = 50 \text{ kg m}^2$
Motorcycle yaw inertia	$I_{zz} = 40 \text{ kg m}^2$
Motorcycle cross inertia	$I_{xz} = 2 \text{ kg m}^2$
Rear wheel rotation inertia	$I_{yr} = 0.8 \text{ kg m}^2$
Front wheel rotation inertia	$I_{yf} = 0.5 \text{ kg m}^2$
Front assembly rotation inertia	$I_\delta = 0.5 \text{ kg m}^2$

Structural properties

Rear tyre radial stiffness	$k_r^r = 1.7e5 \text{ N/m}$
Front tyre radial stiffness	$k_t^r = 1.4e5 \text{ N/m}$
Front and rear tyre radial damping	$c_t = 350 \text{ N s/m}$

Aerodynamic properties

Drag coefficient in standing configuration	$C_D^s = 0.6 \text{ m}^2$
Drag coefficient in prone configuration	$C_D^p = 0.2 \text{ m}^2$
Lift coefficient in standing configuration	$C_L^s = 0.07 \text{ m}^2$
Lift coefficient in prone running configuration	$C_L^p = 0.03 \text{ m}^2$

Other vehicle and rider properties

Rider movement map	$y_r = \begin{cases} 0.05 \cdot \varphi \text{ m} & \text{if } \varphi \leq 0.8 \\ 0.04 \cdot \text{sign}(\varphi) \text{ m} & \text{if } \varphi > 0.8 \end{cases}$
Maximum power	$P_{max} = 180 \text{ kW}$
Steering damper damping	$c_\delta = 15 \text{ N m s/rad}$
